Direct imaging of three-dimensional structure and topology of colloidal gels

2002 J. Phys.: Condens. Matter 14 7581

(http://iopscience.iop.org/0953-8984/14/33/303)

INSTITUTE OF PHYSICS PUBLISHING JOURNAL OF PHYSICS: CONDENSED MATTER

J. Phys.: Condens. Matter **14** (2002) 7581–7597 PII: S0953-8984(02)38648-X

Direct imaging of three-dimensional structure and topology of colloidal gels

A D Dinsmore[1,2] **and D A Weitz**[1]

[1] Department of Physics and DEAS, Harvard University Cambridge, MA 02138, USA
[2] University of Massachusetts Physics Department, Amherst, MA 01003, USA

Received 25 June 2002
Published 9 August 2002
Online at stacks.iop.org/JPhysCM/14/7581

Abstract

We present novel measurements of the structure of colloidal gels. Using confocal microscopy, we obtain the precise three-dimensional positions of a large number of particles. We develop quantitative descriptions of the topology of the gel, including the number of bonds per particle, the chemical or bond fractal dimension, the number of flexible pivot points and other topological parameters that describe the chainlike structure. We investigate the dependence of these parameters on the particle volume fraction and the strength of the attraction that holds the particles together. While all samples have approximately the same fractal and chemical dimensions, we find that gels formed with stronger attraction or larger volume fraction have fewer bonds per particle, more filamentous chains and a greater number of flexible pivot points. Finally, we discuss the topological results in the context of the gel's elasticity. Measurements of the elastic constants of individual chainlike segments are explained with a simple model. The distribution of elastic constants, however, has a general form that is not understood.

(Some figures in this article are in colour only in the electronic version)

Monodisperse colloidal particles have served as a fascinating model system for the study of a wide range of phenomena. Their size is ideal for light scattering, and they have long served as a model system for the development of new scattering techniques, both dynamic and static. They have been important models in the understanding of hydrodynamic interactions and the methods for probing them by scattering. They have also served as a model for the study of phase behaviour of atomic systems, with each colloidal particle playing the role of an atom. The larger size of the colloidal particles compared with atoms and resultant slower diffusive motion make it feasible to use optical scattering techniques to study their behaviour. Thus, they provide a fascinating statistical model system with which to probe the phase behaviour of materials. When the particles interact exclusively through volume exclusion, they behave as hard spheres and exhibit both crystalline and glassy states as their volume fraction is varied.

Upon addition of a high concentration of much smaller particles, an attractive interaction is induced between the particles, and they form a colloidal gel. One of the true leaders in the study of colloidal particles, and in the development of the light scattering techniques which has made their study feasible, is Professor Peter Pusey. He has been a pioneer in the development of the light scattering techniques that have been so important to the study of colloid physics, and he has introduced the essential concepts for the study of both colloidal glasses, and colloidal gels made by depletion interactions.

Much of our understanding about the properties of colloidal particles comes from light scattering studies. This is particularly true for colloidal gels. The randomness of the structure makes the ensemble averaging of light scattering techniques a very valuable probe. The true hallmark of a gel is the existence of a modulus at low frequency, and thus another valuable probe for colloidal gels has been rheology. Great progress has been made in developing an understanding of the elastic behaviour from the scattering data, thereby relating the bulk rheological properties of a gel to the microscopic structure. Unfortunately, however, while light scattering measurements do provide an excellent probe of the ensemble average properties of a colloidal gel, scattering does not provide information about the detailed local structure. A complete understanding of gel rheology, moreover, depends on much more than the average structure; the topology of connections among particles also plays a critical role in the rheogical behaviour of the network.

The goal of this paper is to develop a more detailed picture of the topology of a colloidal gel, and to explore the relationship between topology and the elastic properties of the network. Topological information is not accessible from light scattering data or from rheology. Computer simulations of aggregation have categorized a number of these topological characteristics, including the chemical or bond dimension, which describes the scaling of the contour length with separation, the spectral dimension and some information about structural weak points in the gel [1, 2]. Although these parameters serve as the key inputs to phenomenological models of gel elasticity [3–6], they have not been directly measured to date.

In this paper, we describe detailed measurements of the structure and topology of colloidal gels. We use a confocal microscope to measure the precise three-dimensional positions of thousands of individual particles in the gel. In addition to presenting our data, we describe in detail our methods of quantifying structure and topology. It is useful to describe a gel as an entangled network of chains; the topology of individual chains and the manner of their interconnections together dictate the bulk elasticity. Here we focus on the topology and elasticity of individual chains, each consisting of a sequence of particles bonded to one another. We report on the contour length of chains, their cross-sectional area, their radius of gyration and the number of particles that can freely pivot in all directions without locally stretching bonds. We show how these properties vary in samples with different particle concentrations and strengths of attraction. We also show how these properties dictate the elasticity of individual chains.

1. Samples and experimental procedures

We use poly(methylmethacrylate) (PMMA) particles, dyed with fluorescent rhodamine and suspended in a mixture of decalin and cyclohexylbromide that matches both the density and refractive index of the particles [7, 8]. The particles did not settle to any observable extent after centrifuging at 6000 g for 15 h, confirming the buoyancy match. We report results from ten samples with a variety of particle sizes and concentrations, as detailed in table 1. The mean particle radius, a, was measured with an uncertainty of approximately 0.05 μm from the lattice parameter of close-packed colloidal crystals and from the contact value of the pair distribution function of gelled samples. The measured radius agreed with the value

Table 1. Samples reported here, along with the labels used in the text. $\xi = R_g/a$. 'Fluid-clust' refers to samples that form a fluid of aggregates (see figure 1(a)). 'Gel' refers to samples that form an aggregate of macroscopic size (see figure 1(b)).

Label	c_p	ϕ	a/R_g (nm)	ξ	Description
A	5.1	0.03	350/38	0.11	Fluid-clust
B	5.5	0.03	350/38	0.11	Fluid-clust
C	9.1	0.03	350/38	0.11	Gel
D	12.2	0.03	350/38	0.11	Gel
E	9.3	0.06	350/38	0.11	Gel
F	9.8	0.10	350/38	0.11	Gel
G	6.7	0.05	350/93	0.27	Gel
H	22.3	0.04	750/8.4	0.01	Gel
I	7.2	0.04	750/38	0.05	Gel
J	4.6	0.05	750/93	0.12	Gel

determined by light scattering from particles suspended in dodecane. We determine the particle volume fraction, ϕ, by measuring the number density of particles, and knowing their radius, a. We induce a depletion attraction of controlled strength through the addition of polystyrene (PS, Polymer Laboratories) [9–13]. Three different molecular weights are used to vary the range of the potential, with molecular weights and estimated radii of gyration, R_g, of 96 000 ($R_g = 8.4$ nm), 1.95×10^6 ($R_g = 38$ nm) and 11.6×10^6 ($R_g = 93$ nm). This allows us to vary the ratio of size of the polymer and the size of the spheres, $\xi \equiv R_g/a$. We define the concentration of polymer, c_p, as the mass of polymer, in milligrams, divided by the volume of the solvent, in millilitres (the total volume multiplied by $1 - \phi$). The maximum strength of the depletion attraction, U_{d0}, is numerically approximately equal to c_p, when measured in k_BT, in samples with $a = 350$ nm (samples A–G) and approximately twice c_p in samples with $a = 750$ nm (samples H–J). The process of incorporating the rhodamine dye leaves a charge on the particles, resulting in a long-range repulsion. The magnitude of the electrostatic repulsion is estimated by measuring the gelation time and comparing it with the DLCA model [14]. In samples with $a = 750$ nm (G–J), the estimated charge magnitude lead to a repulsive interaction of $U_C(r) = 0.3k_BT/(r - a_c)$, where a_c is the radius of the sphere corrected for the thickness of the steric layer, whose thickness is about 10 nm [14].

Sample cells consist of a #1$\frac{1}{2}$ cover slip glued to a standard glass microscope slide. Glass spacers are used to construct a gap with 1 mm thickness; the sample area is approximately 10 mm $\times$ 30 mm. Adhesive cured with ultraviolet light (Norland NOA) is used to construct the empty cell. The colloid is injected into the cell through a 3 mm hole, which is subsequently sealed using 5 min epoxy. To avoid contact between the colloid and the wet epoxy, the cell is only filled half-way with colloid. After the epoxy has hardened for at least a day, sample cells are shaken, then placed on the microscope stage within 30 s to verify complete breakup of any aggregates. To avoid disturbance of the sample by motion of the air bubble, samples are left affixed to the sample stage during the observation period, which is typically several days.

Real-space images are collected with a confocal microscope with a scanning slit (Noran Oz). Images are acquired at 15 or 30 frames per second, with pixel sizes of either 0.086 or 0.22 μm in the x- and y-directions. Image stacks typically contain approximately 100 images, each offset by 0.2 μm in the z-direction. Fluorescence is excited using with the 488 nm line of an Ar^+ ion gas laser; the fluorescence is filtered with a 500 nm long-pass filter, and is detected with a photomultiplier tube [8].

Images are analysed using IDL routines to filter the images and locate particle positions in three dimensions [7, 15]. Images with the computer-determined particle positions overlaid are

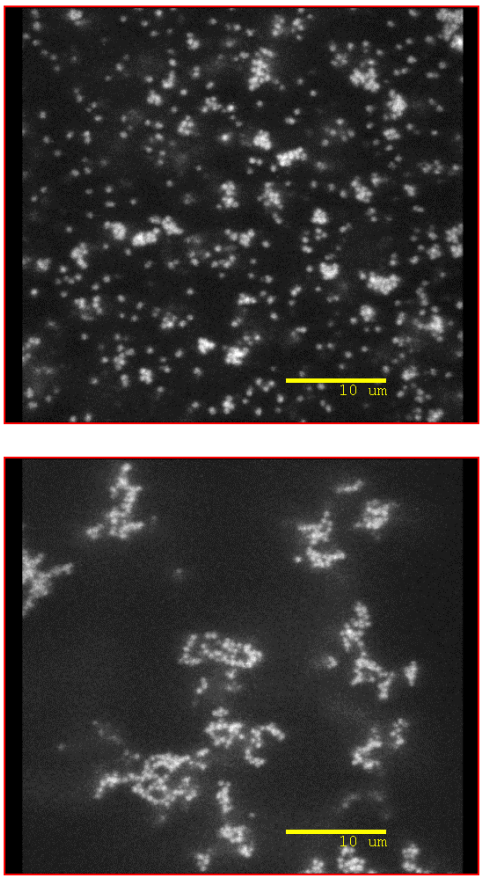

Figure 1. (Top) Confocal microscope image of a thin slice through a sample in the fluid-cluster phase (sample A). (Bottom) Image of a sample that has formed a gel (sample D; 21 h). All of the particles in this image are part of the same cluster. The scale bars represent 10 μm.

routinely checked to ensure accuracy. Each three-dimensional field of view contains between 5000 and 15 000 particles. We estimate that less than $\sim$0.1% of particles are not detected by the software. The uncertainty in the particle positions is estimated to be 50 nm [8].

2. Phase behaviour and aggregation kinetics

In this section, we provide descriptions of the final state of the samples as well as the kinetics of aggregation. Most samples formed colloidal gels. The aggregation is quite slow, presumably owing to the weak, long-range electrostatic repulsion.

2.1. Phase behaviour

All of the ten samples discussed in this article undergo random aggregation; we do not observe any crystalline structures. In table 1, we list the samples discussed here along with their parameters and their final state.

Two samples form a fluid of aggregates of finite size, which we refer to as 'fluid-cluster' samples [13, 16], as shown by a typical image in figure 1(a), which is for sample A, with

$U_{d0} = 5.1$, $\phi = 0.03$, $a = 350$ nm and $R_g = 38$ nm. Clusters that had formed after 5 h remained in suspension for at least 21 h with no further growth in mean cluster size. Sample B ($c_p = 5.5$, $\phi = 0.03$) behaved in a similar way; samples with lower c_p did not aggregate and samples with larger c_p ($U_{d0} > 6$, for $\phi = 0.03$) formed a gel. The underlying origin of the fluid-cluster phase is not clear. The most obvious possibility is that the clusters are in dynamic equilibrium, with cluster formation and breakup occurring at equal rates. However, we never observed a cluster break or a particle spontaneously dissociate from an aggregate. Thus, the origin of this cluster-fluid phase remains uncertain.

All other samples (C–J) formed a gel within the experimentally accessible timescale (≈50 h). An optical micrograph of the cross-section of a typical sample of such a gel is shown in figure 1(b), which is from sample D, after 29 h.

We verified that the depletion-induced aggregation is reversible: clusters melted when c_p was reduced by gentle dilution. To avoid shear-melting the clusters during dilution, we constructed a sample cell containing a compartment isolated by a filter membrane. We then gently added solvent ($c_p = 0$) to one side of the membrane, which protected aggregates within the compartment from convective flow. As the polystyrene polymer diffused out of the compartment through the membrane, clusters dissociated into single particles in a matter of minutes.

2.2. Aggregation kinetics

To study the aggregation kinetics, we homogenize the samples by shaking them, breaking all clusters, as verified by taking images within 30 s. We then acquire a time-lapse series of three-dimensional images to probe the evolution of aggregate structure. The interval between three-dimensional images (typically >30 s) was too large to allow tracking of individual particles from one three-dimensional image to the next. Thus, we monitor the evolution of the clusters, rather than single-particle kinetics. Early in the aggregation process, the clusters were small and numerous, so the finite size of the field of view does not significantly affect the cluster statistics.

We define individual clusters topologically, by finding all particles that are connected to one another through depletion 'bonds'. Bonded particles are identified by their separation. The probability of inter-particle separations r shows a well defined minimum at $r = r^*$, where r^* is slightly larger than $2a + 2R_g$. Particles with separation less than r^* are defined as being bonded.

The mean number of particles per cluster, $\langle n(t) \rangle$, increases approximately linearly with time at early times, when the clusters are small, providing a sufficient number of clusters to obtain reliable statistics. At later times, there are insufficient clusters to reliably determine the growth kinetics. Thus, we find $\langle n(t) \rangle = t/\tau$, for 30 s $< t <$ 300 s. However, the value of τ varies from 10^2 to 10^3 s in samples A–D, which is significantly larger than the diffusion-limited aggregation time, or the average time it takes for two single particles to collide due to diffusion, $\tau_{agg} = R^2_{sphere}/(6\phi D) \approx 5$ s [17]. Linear growth is expected for purely diffusion-limited cluster aggregation (DLCA) [18], and has been observed for DLCA of colloidal gold [19] and for polystyrene spheres [20, 21]. However, in the latter study, while the aggregation time was initially given by τ_{agg}, it then increased to approximately 3.6 τ_{agg} for $t > 15\tau_{agg}$. In our samples the measured aggregation time was even larger, approximately $10^3\tau_{agg}$; this is most likely due to the electrostatic repulsion. By contrast, for samples undergoing reaction-limited cluster aggregation (RLCA) [22], $\langle n(t) \rangle$ is expected to grow exponentially. However, many systems behave in a manner intermediate between these two limiting regimes, and a linear growth of the clusters is often observed in this regime [23, 24]. Thus, it is most likely

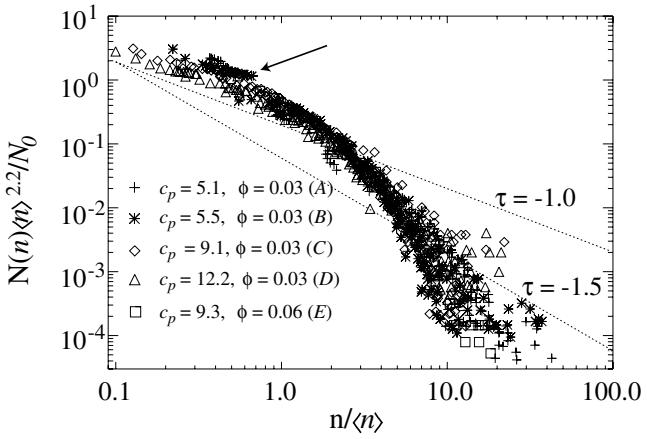

Figure 2. Cluster mass distributions of samples at various times prior to complete gelation. The samples with $c_p = 5.1$ and 5.5 (+, ∗) formed the 'fluid-cluster phase'; other samples formed gels. The scaled cluster-size distributions overlap, except the fluid-cluster samples, which have a slight excess of monomers ($n = 1$) (see arrow). The dashed lines show power-law decays with $\tau = -1.0$ and -1.5.

that these samples are in this intermediate aggregation regime, between the limiting cases of diffusion-and reaction-limited cluster aggregation.

Additional support for the aggregation kinetics comes from the cluster-size distributions, which exhibit scaling behaviour typical of cluster aggregation processes. To demonstrate this, in figure 2 we plot $N(n)\langle n(t)\rangle^{2.2}/N_0$ as a function of $n/\langle n\rangle$, where $N(n)$ is the number of clusters of size n, and N_0 is the total number of particles. For each sample, cluster mass distributions are measured at several times and in several regions within the first several hours of aggregation; these results are all included in the figure. The data all collapse onto a single, time-independent scaling curve, as is typically observed for cluster aggregation; this reflects the fact that aggregation is a conservative process described by a set of rate equations [25, 26]. In computer simulations of aggregation with finite ϕ, this form of the distribution has a time-independent form [27]. As in the simulations, we find the best data collapse after scaling with $\langle n(t)\rangle^{2.2}$, although $\langle n(t)\rangle^{2.1}$ gives very similar results. For DLCA at finite ϕ, the distribution is expected to have an approximate power-law dependence with exponent $\tau = -1.0$; for RLCA, τ is expected to be approximately -1.5. Our results are intermediate between these two powers, again consistent with intermediate aggregation kinetics. Finally, we note that, compared with the samples that gel, the two fluid-cluster phases have an excess of monomers (see arrow), suggesting that these samples might be thought of as a coexistence of aggregated and fluid phases.

The cluster radius scaled with mass with a fractal exponent, as expected for fractal colloidal aggregate. In figure 3, we plot the cluster mass, n, against the radius of gyration of the cluster measured before clusters formed a system-spanning network. We found n is proportional to the radius of gyration raised to power d_f with $d_f = 1.9$–2.0. This value of d_f is consistent with the value obtained for clusters aggregating in the intermediate regime [24]; it is also similar to the value obtained for DLCA at finite volume fraction [27] and finite attraction strength [16, 28–30]. We obtained approximately the same d_f for the fluid-cluster samples (A and B); they are fractal in structure, not compact. Surprisingly, there is no observable increase in d_f in these samples over a period of 21 h, suggesting that there is no significant compaction of the structure over time.

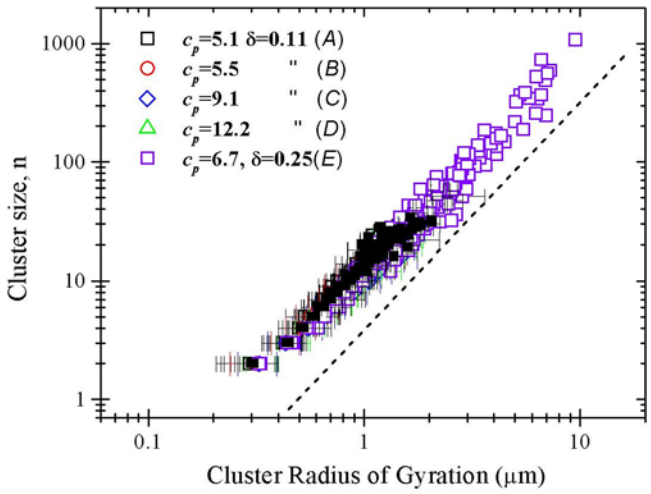

Figure 3. Log-scale plot of the number of particles per cluster (n) as a function of mean cluster radius of gyration. The power-law scaling indicates a fractal dimension $d_f \approx 1.9$; the dashed line indicates $d_f = 2.0$.

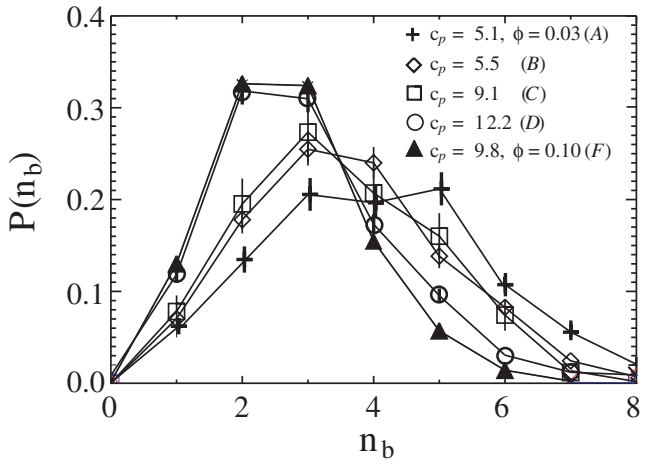

Figure 4. Distribution of number of bonds per particle, n_b. Only particles in clusters containing 20–22 particles are shown. Data were taken 5 h after shaking. Increasing ϕ or c_p tends to reduce n_b.

3. Gel structure and topology

The great advantage of direct imaging of colloidal gels is in the detailed topological information that can be obtained. This provides qualitatively new information that has previously been available only in computer simulations. The new data also call for new methods of analysis to describe this additional information. In this section, we present the results of these topological characterizations. We begin by looking at the bonds around individual particles. We then consider chainlike sections of the gel and study their individual topological properties. Finally, we consider whether the chains form locally rigid structures such as tetrahedra.

3.1. Inter-particle bonds

An important characterization of the local structure is the number of bonds per particle. The evolution of bond number helps determine, for example, whether there is rearrangement at the local scale. Such rearrangement might be expected for depletion bonds, which are centrosymmetric and hence might not resist rotational rearrangement. To investigate the number of bonds per particle, we construct a histogram of bond lengths, and identify a sharp minimum, which we define as the bond cut-off length, r^*. Two particles are then considered bonded if their separation is less than this cut-off length. Particles at the outer edges of clusters will naturally have fewer neighbours, and to avoid biasing the results we restrict our analysis to clusters of similar size, those containing 20–22 particles. This small size was chosen to obtain a statistically significant number of clusters in the fluid-cluster samples, A and B. We plot the distribution of the number of bonds per particle, n_b, in figure 4. Measurements are made 5 h after shaking (prior to complete gelation). The peak of the distributions and the mean values range between 2.7 and 4, substantially lower than in glasses or crystalline solids. Moreover, the distribution systematically shifts toward lower n_b in samples with larger c_p (see data for samples A–D). In equilibrium, one would expect the number of bonds to increase as the inter-particle attraction is strengthened. Gels, however, do not reach equilibrium over the time of the measurements, but remain trapped in a metastable state. Surprisingly, increasing ϕ also leads to a decrease in $\langle n_b \rangle$, even though there are more particles available with which to form bonds (compare samples C and F). In general, samples that lie deeper inside the gel region of the phase diagram have fewer bonds per particle. The number of bonds increases with time, though we were unable to identify any robust functional form for the time dependence. For example, in sample D, the distribution peaks at $n_b = 2$ after 5 h and at $n_b = 3$ after 55 h.

In DLCA, fractal morphology arises because the clusters cannot interpenetrate because of their diffusive motion and strong bonding; thus particles and clusters tend to stick at the outer regions of the growing cluster. If the bonds are rigid and irreversible, then the dominant local topology should be chains, and the bond-number distribution should be peaked at $n_b = 2$ and should not change over time. In all of our samples (except for H [14]), the bonds are centro-symmetric. Thus particles within a cluster can rotate around their bonded partner, leading to reorganization and compaction. This rotational reorganization will be hindered by the larger structure of the aggregate. Hence, the rate of rotational diffusion competes with the rate of aggregation to determine the amount of local reorganization and n_b. In DLCA, the rate of aggregation increases proportional to ϕ [17], while the rate of rotational diffusion of bonded particles depends on the width of their bond. When particles are squeezed closer together due to an increase in U_d, the hydrodynamic friction increases[3]. Thus, in samples with large U_d, rotational diffusion is suppressed relative to cluster growth rate. Consistent with this, $P(n_b = 2)$ monotonically increases with c_p for samples A–D (constant ϕ), as shown in figure 4. Similarly, $P(n_b = 2)$ increases with ϕ owing to the reduction in DCLA aggregation rate (compare C with F).

Figure 5 shows a three-dimensional reconstruction of a section of a gel (sample C). The colours of the spheres indicate the number of bonds, as described in the figure caption. We have also calculated the length-dependent correlation of n_b and found positive correlation among nearest neighbours, weak anti-correlation (~ -0.1) among next-nearest neighbours and zero correlation at longer lengths [8]. The lack of spatial correlation of n_b indicates that the clusters do not consist of locally compact clusters connected by thinner filaments.

[3] The friction between two surface grows like 1/separation for small separation.

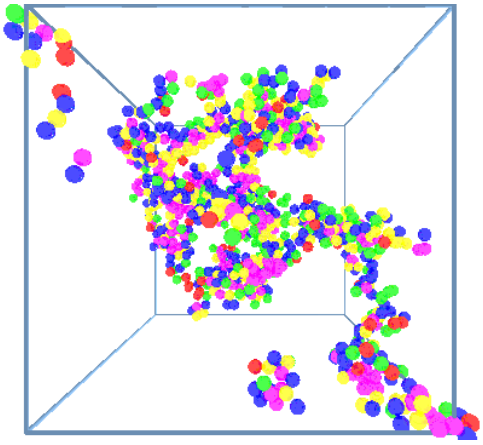

Figure 5. A three-dimensional reconstruction of particles in a colloidal gel (sample C). All of the particles shown here are part of the same cluster; ones near the edge may be bonded to particles outside the field of view. The colours indicate the number of bonds per particle, n_b. Red, $n_b = 0$ or 1; yellow, $n_b = 2$; green, $n_b = 3$; blue, $n_b = 4$; purple, $n_b = 5$ (n_b increases toward the blue end of the colour spectrum). The size of the imaged region is 20 μm × 18 μm × 22 μm. (A colour version of this figure may be found in the electronic version of this article).

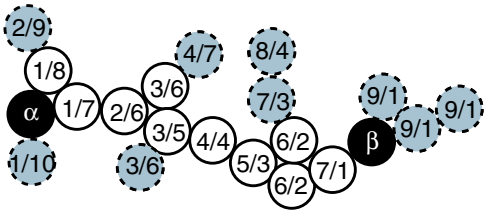

Figure 6. Illustration of a segment of a gel. The numbers indicate the chemical lengths, $L^{\alpha i}$ and $L^{i\beta}$, between each particle and the end-point particles α and β. Clear circles indicate particles for which $L^{\alpha i} + L^{\alpha i} \leqslant L^{\alpha\beta} + 1$. The length $r^{\alpha\beta}$ is defined as the Euclidean length between α and β. Here, $L^{\alpha\beta} = 8$ and $N_{ch}^{\alpha\beta} = 12$.

3.2. Chain topology

The real-space particle positions provide full detail on the connectedness, or topology, of the gel. This information is essential in determining the mechanical strength of the gel, but is not accessible by light scattering, which probes an average of the structural correlations within the cluster. An important measure of the connectivity of the gel is provided by the length of the shortest path or contour length, L, between two arbitrary particles in the same cluster. To determine this, we begin with a single particle, labelled α, and find the nearest neighbours (i), labelled $L^{\alpha i} = 1$, and then the second-nearest neighbours, labelled $L^{\alpha i} = 2$, and so on (see figure 6 for an illustration). In this way, $L^{\alpha\beta}$ is the minimum number of steps needed to move along the gel from particle α to β. The distribution of L values for the largest clusters in sample D is plotted in figure 7(a). Alternative representations are shown in figures 7(b) and (c), which contain scatter plots of L and r for samples D and J, taken from measurements of 4859 and 799 particles, respectively. Also shown are the mean L-values, $\langle L \rangle$. The scaling of this defines the chemical, or bond, fractal dimension, d_b, $\langle L \rangle = Ar^{d_b}$, from which we obtain $A = 2.1$ and $d_b = 1.2 \pm 0.1$ in the samples studied. No systematic variation of d_b with elapsed time, c_p

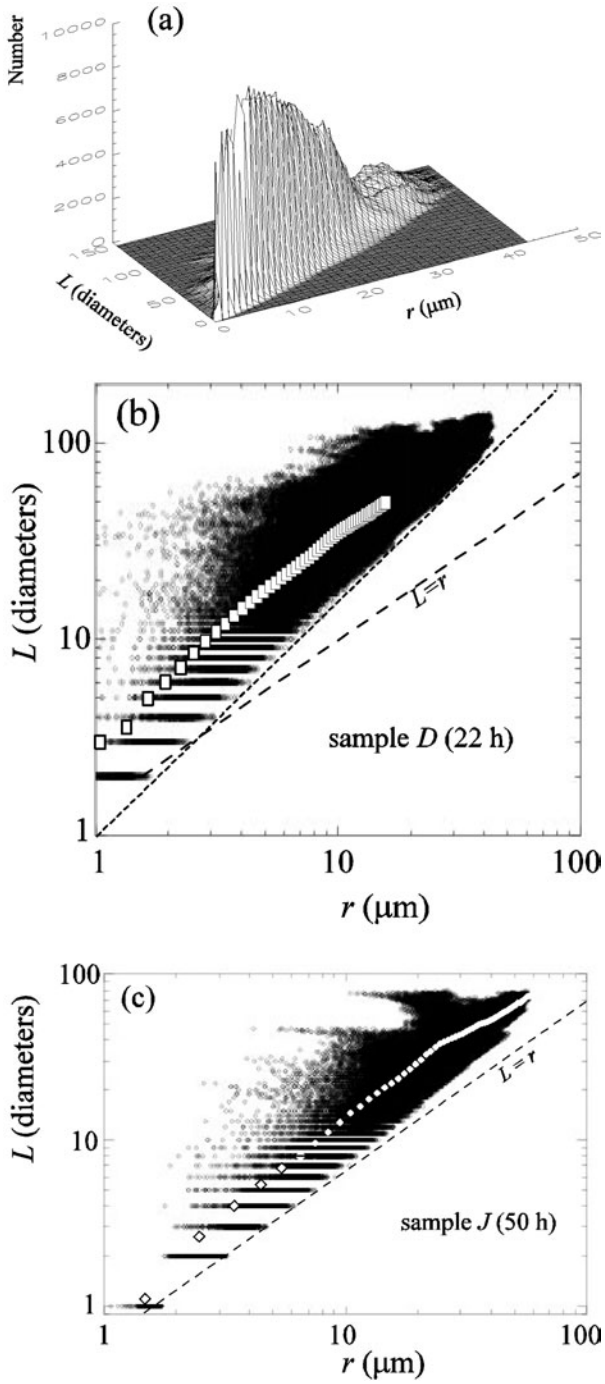

Figure 7. (a) Surface plot of the number of chains as a function of L and r for sample D, at $t = 22$ h. (b) Scatter plot of L and r on a logarithmic scale for the same sample. The slope of the short-dashed line is 1.18. The dashed line indicates $L = r$. The squares show the mean L for each r. (c) Equivalent plot for sample J, at $t = 50$ h. In the samples studied, we found $\langle L \rangle \propto r^{d_b}$ with $d_b = 1.2 \pm 0.1$.

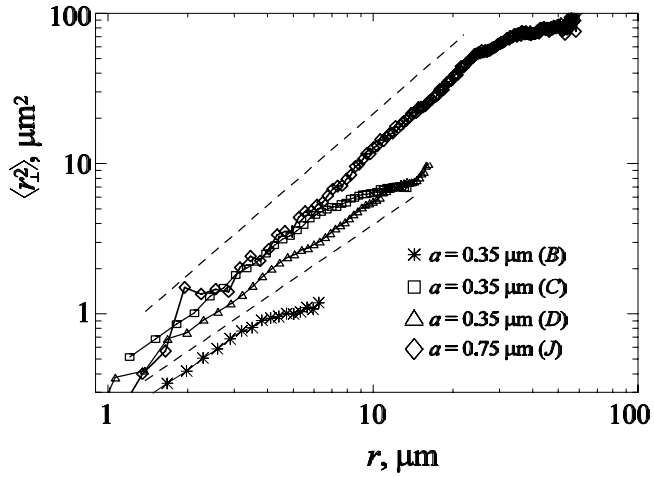

Figure 8. Plot of the mean perpendicular radius of gyration squared, $\langle r_\perp^2 \rangle$, as a function of chain length r for samples B, C, D and J. The dashed lines represent power laws with exponents 1.2 and 1.5.

or ϕ is observed. This measurement of d_b agrees with the results of computer simulations for DLCA gels (with no hydrodynamic interactions) in three dimensions, for which $d_b = 1.25$ [2]. The growth of chains may be modelled as a sequential adsorption of particles that form bond angle θ with respect to the end-to-end axis. In this model, $\langle L \rangle = r/\cos\theta$. By comparison the data give $\theta = 62°$, which is close to the 60° bond angle of close-packed structures.

The data indicate an unexpected result: for each r, there is a well defined *minimum* value of L, which also scales as r^{d_b}. These minimum-length chains—not the mean—might dictate the elastic properties of the gel as a whole. Remarkably, the same value for the chemical dimension describes their length dependence.

As a further measure of the shape of individual chains, we compute the squared radius of gyration for rotation about the end-to-end axis, $r_\perp^2$, and plot the results as a function of r in figure 8. We find $\langle r_\perp^2 \rangle = c(r/a)^\gamma$, with $\gamma = 1.5$ for sample J and $\gamma = 1.2$ for samples B, C and D. A diffusive model, in which chains grow by sequential adsorption of particles with bond angles randomly switching (in two or three dimensions) between θ and $-\theta$, would predict that $\langle r_\perp^2 \rangle$ increases with the number of steps, L. Hence, $\gamma = d_b$. This model agrees with the results for samples B, C and D, and is within the experimental uncertainty for sample J. This behaviour can be contrasted with that expected if the chains grew deterministically, maintaining a uniform curvature or shape, which would result in $\gamma = 2$. The scaling of $\langle r_\perp^2 \rangle$ plays an important role in determining the local elastic properties of the network, as the elasticity of a single chain is dictated by its shape. If a chain is composed of rigid bonds, its elastic constant depends on $1/\langle r_\perp^2 \rangle$; chains containing many kinks and bends have relatively large $\langle r_\perp^2 \rangle$ and weaker elastic constant, while straighter chains have smaller $\langle r_\perp^2 \rangle$ and stronger elastic constants. Thus the perpendicular length plays a critical role [3]. The scaling of $\langle r_\perp^2 \rangle$ with chain length can only be determined by direct imaging methods such as those used here, as scattering is not sensitive to this level of structural detail. It is generally assumed that $\langle r_\perp^2 \rangle \sim r^2$, which is not supported by our data [3, 4, 6]. This modification will have important consequences for the elastic modulus of the gel, as it will change the contribution of the individual clusters to the total modulus.

We also investigate the possibility of structural changes at the local level that might result from the centro-symmetric character of the depletion attraction. For example, local rearrangements might tend to lead to locally tetrahedral structures, which would result in

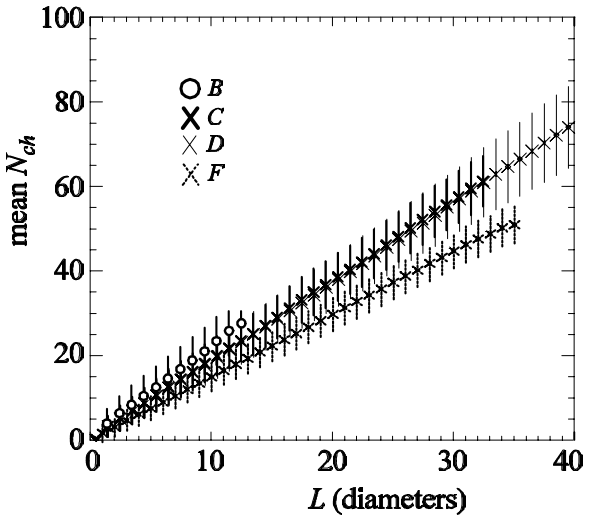

Figure 9. Plot of the mean number of particles in a chain, $\langle N_{ch} \rangle$, as a function of chain length L. Data for samples B, C, D and F are shown (C and D are nearly indistinguishable). The slopes of the lines indicate the mean chain cross-sectional area, which decreased as c_p or ϕ were increased.

an increase in the cross-sectional area of the chain. Therefore, we also quantify the cross-sectional area of each individual chain to look for systematic changes. We define the area of cross section, A_x, by the relation $\langle N_{ch} \rangle = A_x L$, where $\langle N_{ch} \rangle$ is the mean number of particles in a chain of length L—effectively, the volume of the chain. For a given chain, we define N_{ch} as the number of particles i for which $L^{\alpha i} + L^{i\beta} \leqslant L^{\alpha\beta} + 1$, where α and β are the particles at the chain ends (see figure 6). Figure 9 shows a plot of $\langle N_{ch} \rangle$ as a function of L. We find that A_x varies between 1.5 and 2 and systematically decreases as c_p or ϕ are increased. Thus, gels formed by deeper quenches tend to form more filament-like chains. Gels formed near the gel curve adopt a thicker chain morphology, though they have the same fractal and chemical dimensions, d_f and d_b. This observation is consistent with the decreased number of bonds that form as c_p or ϕ are increased.

3.3. Structural rigidity

The elasticity of the gel network depends sensitively on the details of the connectivity of the structure. Weak points or other inhomogeneities can dramatically affect the local strength of the gel. Such localized effects cannot be probed by scattering techniques, but can be directly viewed in real space. However, the relationships among local structural imperfections or weak points, elasticity at intermediate length scales [31] and the macroscopic elasticity are unclear; new analysis methods must be developed to investigate these effects. Here, we search for localized weaker points in the chain, which may have a strong effect on the elasticity of the network. Even if the inter-particle bonds are centro-symmetric, chains can be rigid if particles are stacked in tetrahedra (or in triangles in two dimensions; see figure 10(a)) [6]. However, if some particles behave like universal joints, or *pivots*, then the chain's rigidity can be reduced locally. To determine whether a given particle is a pivot, we find its bonded neighbours. If the set of neighbours forms two or more disconnected clusters, then the particle is defined as a pivot (see figures 10(a), (b)). By this definition, particles with one bond (which form end points) cannot be pivots. We note, however, that non-pivot particles could still rotate along

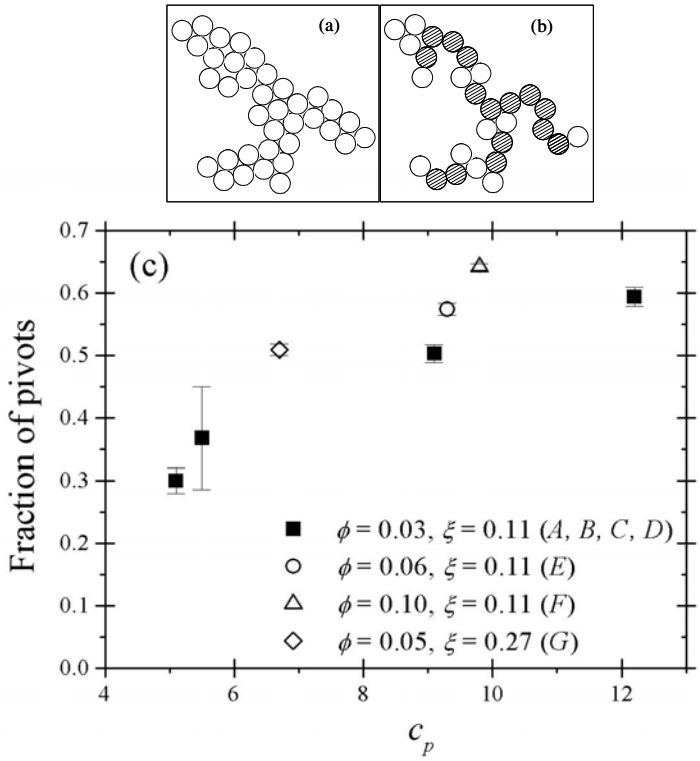

Figure 10. Pivot points in the gel. (a) An illustration of a two-dimensional gel segment with no pivots (as defined in the text). The segment is rigid (for in-plane motion) even if the individual bonds are not. (b) An illustration of a gel segment in which 15 out of 28 particles form pivots (shown as cross-hatched circles). (c) Plot of the measured fraction of 'pivot' particles as a function of c_p for various ϕ and ξ. The fraction of pivots is systematically greater in samples that lie deeper in the gel region of the phase diagram. Data were taken with $t = 18$–22 h and looking only at particles in clusters of 40 or more particles (except sample A, for which $t = 5$ h and the minimum size was 20).

select axes. For example, in the schematic sketch in figure 10(b), the particles can still rotate about axes in the plane of the drawing; thus, absence of pivots does not guarantee that the chain is rigid.

Interestingly, with this definition of rigidity, we found that none of the gels formed structurally rigid chains; they all had a significant fraction of pivots. We illustrate this in figure 10(c), which shows the fraction of particles forming pivots in samples with various ϕ, c_p and ξ. In all cases, at least 30% of particles formed pivots. Moreover, the number of pivots was systematically larger in samples that were more deeply quenched into the gel region of the phase diagram, having larger ϕ or increased c_p. This observation is consistent with the reduction of n_b shown in figure 4. This behaviour implies that a gel can be stable and have a finite shear modulus even with centro-symmetric bonds and non-rigid chains [14]. The stability presumably arises from the multiple links among chains, which prevent further folding and compactification. Furthermore, the stability implies that the chains must be attached to the glass surface at the edge of the cell, presumably by a depletion interaction with the walls. If these surface bonds were cut, then the entire structure would collapse into a denser aggregate

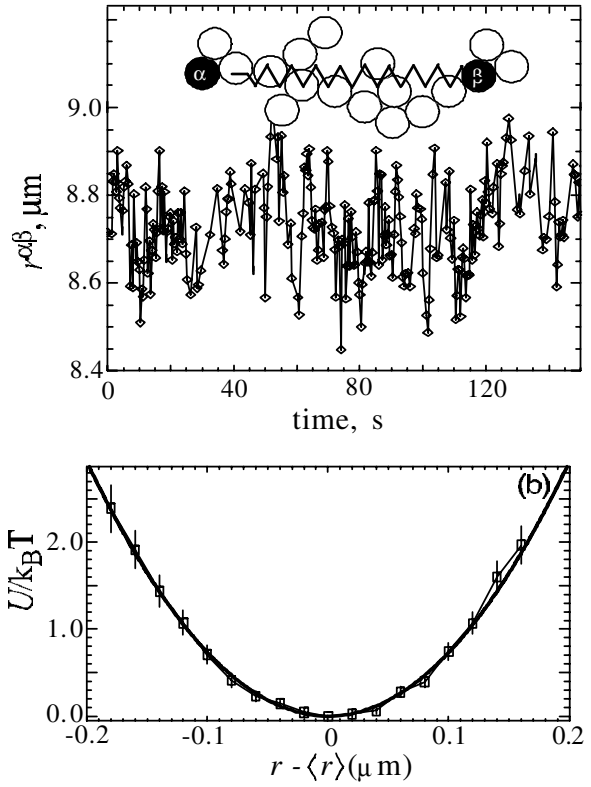

Figure 11. (Top) Plot of separation between two arbitrary particles, $r^{\alpha\beta}$, as a function of time, t. (Bottom) Plot of the measured mean potential between pairs of particles separated by chains with 18 particles ($N_{ch} = 18$). The solid curve is the result of a fit to a parabola, which provides the mean spring constant, $\langle\kappa\rangle = 146 \pm 6k_BT/\mu\text{m}^2$ (sample J).

as the chains bent and folded. Similar behaviour is observed for colloidal gels formed by destabilizing polystyrene particles through the addition of salt [32].

4. Measurements of elastic constants

To help understand the role of the local structure in the elasticity of the network, we measure the local spring constants of the chains. This is accomplished by probing the thermal motion of the particles in a chain; the average magnitude of the fluctuations is determined by the balance of the thermal energy and the energy stored by the elasticity of the chain. This is similar in concept to microrheology, where thermal motion of probe particles can be used to measure the elasticity of the surrounding medium [33]. Similar measurements have also been performed on colloidal gels using dynamic light scattering [34]. However, here, we can probe the local motion directly. To investigate this, we imaged the two-dimensional thermal motions of individual particles in the gel over a period of about an hour. No bond breakage was observed during this period, and the particles maintained a well defined average position. This allowed us to monitor the fluctuations about the average, which provides the detailed information about the elasticity of the network.

We treat the gel as a combination of chains, each acting as a spring, as illustrated in the inset of figure 11(a). By monitoring the separation, r, between two particles, we effectively

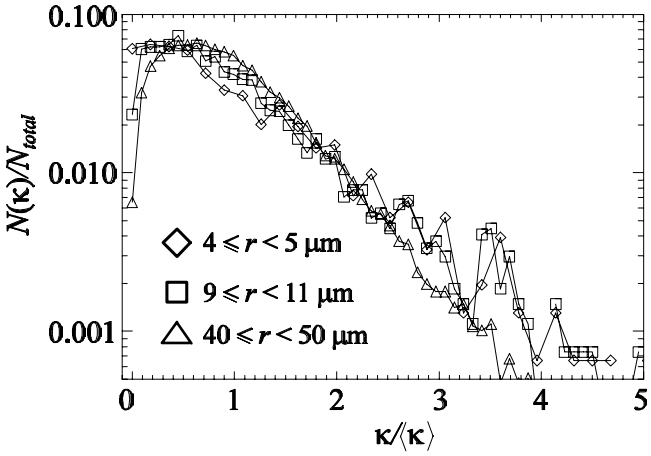

Figure 12. Plot of the distribution of normalized spring constants, $\kappa/\langle\kappa\rangle$, for sample J. The different data points refer to chains of different lengths, r. The vertical axis shows the number of chains with a particular κ divided by the total number of chains. The value of $\langle\kappa\rangle$ is computed from the data. At all length scales, the tail of the distribution falls off as $\exp(-1.5)$.

monitor the end-to-end displacements of a chain segment, as illustrated in figure 11(a). Since the particles are fluctuating in a stationary potential, the probability of separation r is given by the Boltzmann distribution: $P(r) \sim \exp(-U(r)/k_BT)$. Using the trajectories $r(t)$, we histogram r to obtain $P(r)$ and take the logarithm to find $U(r)$. This analysis is done for each pair of particles in the field of view. The $U(r)$ are then sorted according to the properties of the chain, and then averaged. For example, figure 11(b) shows a plot of $U(r - \langle r\rangle)$, averaged over all chains in the field of view for which $N_{ch} = 18$. In general, when $r > 6a$, the chains behaved like linear springs, with quadratic $U(r)$, for displacements up to 0.15–0.2 μm, a strain of as much as 5%. For larger displacements—either contractions or dilations—the springs became softer.

From these data, we are able to measure the length dependence of the spring constant of the chains, $\kappa(r)$, and the dependence of the *mean* values on r, L, N_{ch} and $r_\perp^2$ [14]. In samples with $a = 0.75$ μm and $R_g = 38$ or 93 nm (including samples I and J), we find that $\kappa = \kappa_0/N_{ch}$, where κ_0 is the spring constant of an individual inter-particle bond. This is the result expected for a one-dimensional series of springs. We find that κ does not depend on $r_\perp$. Together these results indicate that the gel is composed of freely jointed chains whose elasticity arises from bond stretching. By contrast, when the depletion attraction is strong and short ranged, as in sample H, the measured κ scales with $1/(N_{ch}r_\perp^2)$, as expected when the elasticity arises from resistance to bond bending. We surmise that, in this case, the bond rigidity arises from the very small separation between particles, which compresses the stabilizing polymer layer, or brings surface asperities into contact, resulting in a resistance to bond bending.

The *distribution* of κ-values provides further insight into the nature of a gel. In figure 12, we plot the distribution of κ-values in sample J, normalized by the average value, $\langle\kappa\rangle$, for all pairs of particles with 4 μm $\leqslant r <$ 5 μm (diamonds), 9 μm $\leqslant r <$ 11 μm (squares) and 40 μm $\leqslant r <$ 50 μm (triangles). The measured values for $\langle\kappa\rangle$ are 87, 33 and 19 k_BT/μm^2, respectively. The distribution is not symmetric; it has a sharp peak and a tail that falls off like $\exp(-1.5\kappa/\langle\kappa\rangle)$. The results for different length scales overlap remarkably well, suggesting that the disorder is independent of length scale. We note, however, that $N(\kappa < \langle\kappa\rangle)$ systematically decreases with r: the ensemble of longer chains has fewer weak ones, possibly

because their small κ leads to thermal breakage before the measurement is made. The data shown in figure 12 are taken 3.5 h after shaking. After 50 h, the distribution is more sharply peaked but the tail is still exponential, with a similar slope. The underlying origin of this exponential distribution of spring constants is not clear. However, it is interesting to note that this distribution of spring constants will lead to an equivalent exponential distribution of forces in the gel upon application of a load. Such an exponential distribution of forces is also the hallmark of jammed systems [35, 36], and a colloidal gel can be considered a jammed system of attractive particles [37].

5. Summary and conclusions

We have presented a detailed study of the topological properties of colloidal gels formed by aggregation due to the depletion interaction, and exploiting direct imaging of the three-dimensional structure using a confocal microscope. We show that the microscopic structure of the gel is systematically more compact in samples with weaker depletion attractions. The number of bonds per particle is peaked at 2 in samples with very strong attraction. The peak shifts to values as large as 5 over time, or when the attraction is weaker or ϕ is smaller. Moreover, we show that the gel may be viewed as a network of chains whose chemical or bond dimension is $d_b = 1.2 \pm 0.1$. For pairs of particles a distance r apart, the *mean* chemical length is $\langle L \rangle = 2.1 r^{d_b}$. Surprisingly, we also find that the *minimum* length $L_{\min}$ for all pairs with separation r also scales with r^{d_b}. The squared perpendicular radius of gyration, $r_\perp^2$, also scaled with r^{d_b}, not r^2, consistent with a simple diffusive-growth picture. Upon analysing the structural rigidity of individual chains, we found that more than 30% of all particles formed freely flexible joints, or 'pivots.' Moreover, the relative number of pivots was larger in samples with stronger attraction or larger volume fraction. Together, these results quantitatively show how a stronger inter-particle attraction leads to a slowing of compaction during aggregation, possibly due to the increased hydrodynamic friction between bonded particles. Finally, we demonstrate that the elastic constants of individual chains could be directly measured and compared with topology. While the mean values of the elastic constants could be understood using a simple elastic model for isolated chains, the distribution of elastic constants followed a scale-invariant form for which we have no explanation. The results show that three-dimensional confocal microscopy can be used to obtain an unusually precise view of the topology and elasticity of colloidal gels.

Acknowledgments

We thank Andy Schofield, who made the colloidal particles used in these experiments. This work was supported by the NSF (DMR-9971432) and by NASA (NAG3-2284 and NAG3-2492).

References

[1] Meakin P 1983 *Phys. Rev. Lett.* **51** 1119
[2] Meakin P, Majid I, Havlin S and Stanley H E 1984 *J. Phys. A: Math. Gen.* **17** L975
[3] Kantor Y and Webman I 1984 *Phys. Rev. Lett.* **52** 1891
[4] Shih W-H *et al* 1990 *Phys. Rev.* A **42** 4772
[5] Potanin A A, de Rooij R, van den Ende D and Mellema J 1995 *J. Chem. Phys.* **102** 5845
[6] Potanin A A and Russel W B 1996 *Phys. Rev.* E **53** 3702
[7] Weeks E R *et al* 1999 *Science* **287** 627
[8] Dinsmore A D *et al* 2001 *Appl. Opt.* **40** 4152

[9] Ilett S M, Orrock A, Poon W C K and Pusey P N 1995 *Phys. Rev.* E **51** 1344
[10] Poon W C K *et al* 1993 *J. Physique* **3** 1075
[11] Poon W C K, Pirie A D and Pusey P N 1995 *Faraday Discuss.* **101** 65
[12] Pusey P N, Pirie A D and Poon W C K 1993 *Physica* A **201** 322
[13] Segre P N, Prasad V, Schofield A B and Weit D A 2001 *Phys. Rev. Lett.* **86** 6042
[14] Dinsmore A D, Prasad V, Wong I and Weitz D A to be submitted
[15] Crocker J C and Grier D G 1996 *J. Colloid Interface Sci.* **179** 298
[16] Haw M D, Sievwright M, Poon W C K and Pusey P N 1995 *Adv. Colloid Interface Sci.* **62** 1
[17] Carpineti M and Giglio M 1993 *Adv. Colloid Interface Sci.* **46** 73
[18] Lin M Y *et al* 1989 *Nature* **339** 360
[19] Weitz D A, Huang J S, Lin M Y and Sung J 1984 *Phys. Rev. Lett.* **53** 1657
[20] Broide M and Cohen R 1990 *Phys. Rev. Lett.* **64** 2026
[21] Broide M L and Cohen R J 1992 *J. Colloid Interface Sci.* **153** 493
[22] Meakin P and Family F 1988 *Phys. Rev.* A **38** 2110
[23] Weitz D A, Huang J S, Lin M Y and Sung J 1985 *Phys. Rev. Lett.* **54** 1416
[24] Asnaghi D, Carpineti M, Giglio M and Sozzi M 1992 *Phys. Rev.* A **45** 1018
[25] van Dongen P G J and Ernst M H 1985 *Phys. Rev. Lett.* **54** 1396
[26] Weitz D A and Lin M Y 1986 *Phys. Rev. Lett.* **57** 2037
[27] Lach-hab M, Gonzalez A E and Blaisten-Barojas E 1996 *Phys. Rev.* E **54** 5456
[28] Kolb M 1984 *Phys. Rev. Lett.* **53** 1653
[29] Shih W Y, Liu J, Shih W H and Aksay I A 1991 *J. Stat. Phys.* **62** 961
[30] Burns J L, Yan Y D, Jameson G J and Biggs S 2000 *Colloid Surf.* A **162** 265
[31] Evans R M L and Starrs L 2002 *J. Phys.: Condens. Matter* **14** 2507
[32] Cipelletti L, Manley S, Ball R C and Weitz D A 2000 *Phys. Rev. Lett.* **84** 2275
[33] Mason T G and Weitz D A 1995 *Phys. Rev. Lett.* **74** 1250
[34] Krall A H and Weitz D A 1998 *Phys. Rev. Lett.* **80** 778
[35] Liu A J and Nagel S R 1998 *Nature* **396** 21
[36] O'Hern C S, Langer S A, Liu A J and Nagel S R 2001 *Phys. Rev. Lett.* **86** 111
[37] Trappe V *et al* 2001 *Nature* **411** 772